

Trial wave functions for ring-trapped ions and neutral atoms: Microscopic description of the quantum space-time crystal

Constantine Yannouleas* and Uzi Landman†

School of Physics, Georgia Institute of Technology, Atlanta, Georgia 30332-0430

(Dated: 21 September 2017)

A constructive theoretical platform for the description of quantum space-time crystals uncovers for N interacting and ring-confined rotating particles the existence of low-lying states with proper space-time crystal behavior. The construction of the corresponding many-body trial wave functions proceeds first via symmetry breaking at the mean-field level followed by symmetry restoration using projection techniques. The ensuing correlated many-body wave functions are stationary states and preserve the rotational symmetries, and at the same time they reflect the point-group symmetries of the mean-field crystals. This behavior results in the emergence of sequences of select magic angular momenta L_m . For angular-momenta away from the magic values, the trial functions vanish. Symmetry breaking beyond mean field can be induced by superpositions of such good- L_m many-body stationary states. We show that superposing a pair of adjacent magic angular momenta states leads to formation of special broken-symmetry states exhibiting quantum space-time-crystal behavior. In particular, the corresponding particle densities rotate around the ring, showing undamped and nondispersed periodic crystalline evolution in both space and time. The experimental synthesis of such quantum space-time-crystal wave packets is predicted to be favored in the vicinity of ground-state energy crossings of the Aharonov-Bohm-type spectra accessed via an externally applied magnetic field. These results are illustrated here for Coulomb-repelling fermionic ions and for a lump of contact-interaction attracting bosons.

I. INTRODUCTION

Groundbreaking experimental progress [1–11] in the field of trapped ultracold ions and neutral atoms, in particular the unprecedented control of interparticle interactions and the attainment of ultracold temperatures, offer these systems as prime resources for experimental realization of the emergent exciting concept of a quantum space-time crystal (QSTC). Inspired by the relativistic 3+1-dimensions analogy [12], the QSTC idea extends translational symmetry breaking (SB) to encompass both the spatial and time dimensions. Indeed, the original QSTC proposal [12, 13] motivated an abundance of scientific discussion, commentary, and exploration [14–24].

The original QSTC was proposed in the form of crystalline spatial-particle-density arrangements [13], or other solitonic-type (charge-density-wave) formations [12] revolving around a ring-shaped ultracold trap without dispersion or damping. Although significant experimental progress has been reported toward this goal [5, 6], formation of a QSTC in this experimental configuration is yet to be demonstrated. At the same time, experimental progress for a “weaker class” [25] of discrete-time-crystals [20–24] limited exclusively to the time domain has been reported [26, 27], employing time-periodically-driven spin systems. Contributing to this state of affairs are limitations of earlier theoretical treatments of the QSTC that were discussed extensively in previous commentary [14–16, 19], e.g., limiting oneself to mean-field (MF) dynamics [12], or considering solely the ener-

getics of states with good total angular momenta which (as a matter of principle) have uniform spatial densities [13, 28]. To throw further light on the nature and properties of QSTCs, it is imperative that a formulation and implementation of appropriate many-body trial wave functions for the QSTC on a ring be advanced. The sought-after trial wave functions should explore for a finite system of N particles the interplay [29] between the mean-field symmetry-broken states, which are not eigenstates of the total angular momentum \hat{L} , and the exact symmetry-preserving (good total-angular-momentum) states.

Here, we introduce such trial wave functions and analyze their spectra and combined spatially dispersionless and temporally undamped evolution, which are the defining characteristics of a QSTC. Contrasting with these findings, previous beyond-mean-field theoretical studies [30–34] that investigated spatial solitonic formations in finite boson systems in one dimension or on a ring have revealed drastically different behaviors, such as increasing dispersion with time accompanied by a revival at the initial position of the propagated inhomogeneous wave packet [35].

We employ a beyond-mean-field methodology of symmetry restoration via projection techniques, introduced by us previously [29, 36–44] for two-dimensional semiconductor quantum dots (with and without an applied magnetic field \mathbf{B}). The multilevel symmetry-breaking and symmetry-restoration approach which we pursue provides a complete theoretical framework for treating symmetry breaking aspects in finite systems, without reference to the $N \rightarrow \infty$ limit. Indeed this approach originated, and is widely employed, in nuclear physics and chemistry [29, 45–53].

* Constantine.Yannouleas@physics.gatech.edu

† Uzi.Landman@physics.gatech.edu

The paper is organized as follows. In Section II we introduce and illustrate the hierarchical, multilevel methodology that we use for the construction of the trial wave functions for the microscopic many-body Hamiltonian of few ultracold ring-confined interacting particles. Following a short synopsis of the method, we discuss first in section II A the mean-field, broken-symmetry state, and subsequently in section II B a beyond-mean-field level is outlined, entailing symmetry-restoration via the use of an angular momentum projection technique. This results in many-body stationary-state good-angular-momentum solutions of the microscopic Hamiltonian. These (projected) symmetry-restored states show uniform particle density around the ring. However, simultaneously they possess hidden crystalline symmetries which can be revealed through the analysis of the corresponding conditional probability densities. In section III C we complete our exposition of the construction of the QSTC trial wave functions by analyzing the properties of superpositions of pairs of the above-noted symmetry-restored (projected) stationary states [see Eq. (1)] that are favored to mix in the vicinity of crossings of Aharonov-Bohm-type spectra of ground-state energies versus applied magnetic-field (Fig. 1). The particle density corresponding to such superposed wavefunctions reveals crystalline structure on the ring. Numerical solutions using the trial wave functions are illustrated and analyzed for the case of few (even and odd in number) Coulomb-repelling fermionic ions, and for a lump of contact-interacting attractive bosons. When evolved with the microscopic many-body Hamiltonian, these trial functions exhibit, for both the fermionic repelling ions and attracting bosons, undamped and non-dispersive space and time crystalline periodic evolution – that is, they exhibit breaking of both the space and time symmetries.

Section III is devoted to further elaboration on three main topics. In section III A we discuss the symmetry properties of the symmetry-restored (projected) wave functions and the selection rules for their “magic” angular momenta. Section III B analyzes the properties of the initial wave packets and their associated time evolution, and section III C comments on the relation between the constructed trial functions (in particular the aforementioned symmetry-restored stationary states) and the wavefunctions obtained through exact-diagonalization [configuration-interaction (CI)] solutions of the microscopic many-body Hamiltonian.

We conclude in section IV with a summary of our work, including a brief listing of recent progress achieved in developing experimental techniques for preparation and measurement of ring-confined ultracold particles. The Appendices give tables of numerical results (rotational energies for different magic angular momenta, and moments of inertia) for the systems investigated in the paper, as well as explicit expressions for the conditional probability distribution and single particle density.

II. THE INTERPLAY BETWEEN SYMMETRY-BROKEN AND SYMMETRY-PRESERVING STATES: GROUP-THEORETICAL FORMULATION

In connection with the QSTC, we consider three levels of many-body trial wave functions: (1) A Slater determinant for localized fermions (or permanent for localized bosons) on the ring. We denote this wave function by Ψ^{SB} ; it corresponds to the unrestricted Hartree-Fock (UHF), or Gross-Pitaevskii (GP), mean-field step [29] that exhibits symmetry breaking of the space degrees of freedom. Ψ^{SB} does not preserve the total angular momentum. Out of the three levels in the hierarchical scheme (see below), it is the trial wave function closest to the familiar concept of a classical Wigner crystal [54]. (2) A stationary multideterminantal (multipermanental) wave function Φ_L^{PROJ} characterized by a good total angular momentum $\hbar L$, which is generated by applying a projection operator \mathcal{P}_L (see below) on Ψ^{SB} . This step goes beyond the MF approximation and restores (as required) the quantum many-body Hamiltonian symmetries in the stationary-state solutions. Unlike Ψ^{SB} , Φ_L^{PROJ} exhibits an azimuthally uniform single-particle density [SPD, $\rho(\mathbf{r}, t)$], which is also time-independent (stationary). Previously, we referred to such projected wave functions Φ_L^{PROJ} as quantum rotating Wigner molecules [43]. (3) Coupling between the stationary states (brought about by a perturbation which we term in the following as “the pinning agent”) results in a superposition of two projected wave functions with different angular momenta L_1 and L_2 , leading to formation of a pinned Wigner molecule (PWM), i.e.,

$$\Phi^{\text{PWM}}(L_1, L_2; t = 0) = \alpha \Phi_{L_1}^{\text{PROJ}} + \beta e^{i\phi(t=0)} \Phi_{L_2}^{\text{PROJ}}, \quad (1)$$

where $\phi(t = 0)$ can be set to zero without loss of generality, and $\alpha^2 + \beta^2 = 1$. In the following we illustrate the case of $\alpha = \beta = 1/\sqrt{2}$ (the physics of the PWM maintains for other choices of the mixing coefficients). For selected magic (see below) L_1 and L_2 , $\Phi^{\text{PWM}}(L_1, L_2; t = 0)$ represent a special family of quantal wave packets with broken azimuthal symmetry. Consequently their corresponding $\rho(\mathbf{r}, t = 0)$ are not uniform, forming instead a crystal-like particle density pattern, with kN , $k = 1, 2, 3, \dots$ possible peaks for N fermionic ions and $1, 2, 3, \dots$ possible peaks for N attractive bosons. When the pinning agent is lifted, the $\Phi^{\text{PWM}}(L_1, L_2; t)$ evolve in time undamped according to the exact many-body quantum Hamiltonian dynamics, i.e., the phase ϕ will vary as $\phi(t) = (E_2 - E_1)t/\hbar$, and the associated $\rho(\mathbf{r}, t)$ will oscillate at any given space point with a time period $T = \tau/n$; $\tau = 2\pi\hbar/|E_1 - E_2|$, $E_{1(2)}$ being the energies of the stationary states $\Phi_{L_i}^{\text{PROJ}}$ with $i = 1, 2$, respectively. For either statistics (fermions or bosons), $n = N$ for repelling ions and $n = 1$ for attractive particles; as aforementioned, here we discuss explicitly Coulomb-repelling fermionic ions and contact-interacting attractive bosons. Such undamped and dispersionless periodic

time variation is not possible for the MF Hartree-Fock (or Gross-Pitaevskii) wave packet Ψ^{SB} , because it contains all the possible angular momenta when expanded in the complete basis set of the stationary wave functions Φ_L^{PROJ} . Additionally, the MF wave functions lose [55] their single-determinant (single-permanent) character under the exact time evolution.

The many-body Hamiltonian of N identical particles in a ring-type trap threaded by a constant magnetic field \mathbf{B} is

$$\mathcal{H} = \sum_{i=1}^N \left(\frac{(\mathbf{p}_i - \eta \mathbf{A}_i)^2}{2M} + \frac{(r_i - R)^2}{2l_0^2/(\hbar\omega_0)} \right) + \sum_{i<j} V(r_{ij}), \quad (2)$$

where $\mathbf{A}(\mathbf{r}) = \mathbf{B} \times \mathbf{r}/2$ is the vector potential in the symmetric gauge, $r = \sqrt{x^2 + y^2}$, ω_0 is the frequency of the trap, $R = \sqrt{X^2 + Y^2}$ is the ring radius, the oscillator length $l_0 = \sqrt{\hbar/(M\omega_0)}$, and $r_{ij} = |\mathbf{r}_i - \mathbf{r}_j|$. \mathbf{B} can be the familiar magnetic field in the case of charged ions (when $\eta = e/c$), or a synthetic one in the case of ultracold neutral atoms [3].

A. First level: The mean-field-ansatz, symmetry-broken crystalline state

In view of the strong inter-particle interactions (large values of the parameters R_W and R_δ , see below) associated with the proposed experimental realizations of the QSTC's [12, 13], resulting, for ultracold quasi-1D-ring-trapped particles, in formation of a Wigner crystal (in the case of Coulomb repelling ultracold ions) or a lump (in the case of contact attracting bosons), we construct here the symmetry-broken initial state via the use of an ansatz. This ansatz explores the localized nature of the N space orbitals (corresponding to the N ring-trapped particles) from which the single broken-symmetry determinant (permanent) is formed in the corresponding fermion (boson) systems. Such ansatz proved most adequate to approximate broken-symmetry mean-field solutions (reflecting individual particle localization) in previous studies of fermions and bosons in harmonically confined quantum dots and other 2D systems [29, 56].

We describe each particle localized at position \mathbf{R}_j as a displaced Gaussian function

$$u(\mathbf{r}, \mathbf{R}_j) = \frac{1}{\sqrt{\pi}\lambda} \exp\left(-\frac{(\mathbf{r} - \mathbf{R}_j)^2}{2\lambda^2} - i\varphi(\mathbf{r}, \mathbf{R}_j; B)\right), \quad (3)$$

with $\lambda = \sqrt{\hbar/(M\Omega)}$; $\Omega = \sqrt{\omega_0^2 + \omega_c^2/4}$ where $\omega_c = \eta B/M$ is the cyclotron frequency. The phase in Eq. (3) is due to the gauge invariance of magnetic translations [57, 58]) and is given by $\varphi(\mathbf{r}, \mathbf{R}_j; B) = (xY_j - yX_j)/(2l_B^2)$, with $l_B = \sqrt{\hbar/(\eta B)}$ being the magnetic length. For simplicity, in the following we provide examples for only three cases: (i) that of N fully polarized fermionic ions with odd N , (ii) that of N fully polarized fermionic ions

with even N , and (iii) that of N spinless bosons interacting via an attractive contact potential. As will be shown explicitly, case (ii) presents different characteristics compared to case (i).

In the case of ultracold ions repelling each other via the Coulomb interaction, we take the $\mathbf{R}_j = R_{\text{eq}} e^{2\pi(j-1)i/N}$, $j = 1, 2, \dots, N$ to coincide with the equilibrium positions (forming a regular polygon) of N classical charges inside the annular confinement specified in Eq. (2). Then $R_{\text{eq}} (> R)$ is given by the real solution of the cubic equation $aw^3 + bw^2 + d = 0$, where $a = 1$, $b = -R$, $d = -l_0^3 R_W S_N/4$, with the Wigner parameter (the ratio between the characteristic interparticle repulsion and the kinetic zero-point energy of the ring-confined particle), $R_W = e^2/(l_0 \hbar \omega_0)$ [29] and $S_N = \sum_{j=2}^N 1/\sin[(j-1)\pi/N]$. Then the corresponding MF wave function, Ψ^{SB} , is the determinant formed by the N orbitals $u(\mathbf{r}_i, \mathbf{R}_j)$.

In the case of N ultracold neutral bosons attracting each other with a contact interaction $-g\delta(\mathbf{r}_i - \mathbf{r}_j)$, the atoms are localized at the same position, and thus $R_{\text{eq}} = R$ and $R_j = R e^{i\theta_0}$, $j = 1, 2, \dots, N$. Then the MF wave function, Ψ^{SB} , is the product (permanent) of the orbitals $u(\mathbf{r}_i, R e^{i\theta_0})$. The parameter corresponding to R_W is given here by $R_\delta = gM/\hbar^2$.

B. Second level (beyond mean field): The projected, symmetry-restored stationary state

A stationary many-body state that preserves the total angular momentum, as well as the rotational symmetry of the annular trap, can be projected out of the symmetry-broken Ψ^{SB} by applying the projector operator \mathcal{P}_L ,

$$\mathcal{P}_L = \frac{1}{2\pi} \int_0^{2\pi} e^{i\gamma(L - \hat{L})} d\gamma, \quad (4)$$

where $\hat{L} = \sum_{i=1}^N \hat{l}_i$, $i = 1, 2, \dots, N$, and $\hbar\hat{L}$ is the total angular-momentum operator. Then the projected many-body state is given by

$$\Phi_L^{\text{PROJ}} = \frac{1}{2\pi} \int_0^{2\pi} d\gamma \Psi^{\text{SB}}(\gamma) e^{i\gamma L}. \quad (5)$$

\mathcal{P}_L is analogous to the projector operators used in chemistry for molecular orbitals governed by point group symmetries [39, 59–61]. Such projection operators are constructed through a summation over the characters of the point group [39, 60, 61]; the phases $e^{i\gamma L}$ are the characters of the rotational group in two dimensions [39, 61] and the operator $e^{-i\gamma\hat{L}}$ is the corresponding generator of 2D rotations. Alternatively, Eq. (5) may be viewed as a linear superposition of all the (energy-degenerate) symmetry-broken states $\Psi^{\text{SB}}(\gamma)$, azimuthally rotated by γ . Due to the rotational symmetry, the coefficients of this superposition, i.e., the phases $e^{i\gamma L}$, can be determined a priori, without the need to diagonalize a Hamiltonian matrix.

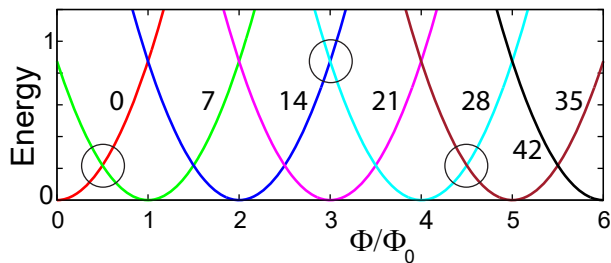


FIG. 1. Aharonov-Bohm-type, quantum-rigid-rotor energy spectrum [second term in the right-hand-side of Eq. (10)] as a function of the magnetic flux through the ring, Φ/Φ_0 , for the symmetry-restored (stationary) states Φ_L^{PROJ} for $N = 7$ fermionic ions. The remaining parameters are: Wigner parameter $R_W = 1000$, ring radius $R = 200l_0$, and oscillator strength $l_0 = 50$ nm. According to Table I in the Appendix A, the parameter C_R in Eq. (10) was taken equal to $1.7847 \times 10^{-6} \hbar\omega_0$. Each curve is labeled with the corresponding magic total angular momentum L_m . The circles highlight several energy-crossing points most susceptible to symmetry breaking. Energies in units of $10^{-4} \hbar\omega_0$.

The projected energies, associated with the stationary wave functions Φ_L^{PROJ} , are given by

$$E^{\text{PROJ}}(L) = \int_0^{2\pi} h(\gamma) e^{i\gamma L} d\gamma / \int_0^{2\pi} n(\gamma) e^{i\gamma L} d\gamma, \quad (6)$$

where

$$h(\gamma) = \langle \Psi^{\text{SB}}(0) | \mathcal{H} | \Psi^{\text{SB}}(\gamma) \rangle, \quad (7)$$

and the norm overlap

$$n(\gamma) = \langle \Psi^{\text{SB}}(0) | \Psi^{\text{SB}}(\gamma) \rangle \quad (8)$$

enforces proper normalization of Φ_L^{PROJ} . Note that the original double integration reduces to a single integration over γ because $\mathcal{P}_L^2 = \mathcal{P}_L$, $[\mathcal{P}_L, \mathcal{H}] = 0$. We note that the unrestricted HF energies for the ansatz determinant (or permanent), Ψ^{SB} , before projection are simply given by

$$E_{\text{UHF}} = h(0)/n(0). \quad (9)$$

We have carried out numerical calculations to determine the rotational spectrum of the Φ_L^{PROJ} 's. For the calculation of $h(\gamma)$ and $n(\gamma)$, we use the rules for determinants composed of nonorthogonal orbitals; see, e.g., Ref. [62]. Similar rules apply for permanents. The numerical calculations are facilitated by the fact that the one-body and two-body matrix elements between the orbitals $u(\mathbf{r}, \mathbf{R}_j)$ have closed analytic expressions [63–65].

In all three cases [(i) odd number of repelling fermions, (ii) even number of repelling fermions, and (iii) attractive bosons], and for all values of $N \leq 10$, large localization parameters $R_W \geq 200$ and $R_\delta \geq 50$, and large ratios $R/l_0 \geq 40$ that we studied, we found that indeed the numerically calculated energies of the Φ_L^{PROJ} 's according

to Eq. (6) (see, e.g., Tables I, II, and III in Appendix A) can be well-fitted by that of an Aharonov-Bohm-type spectrum associated with a quantum many-body rigid rotor (see also [13, 35]), i.e.,

$$E^{\text{PROJ}}(L) \approx V_{\text{int}} + C_R(L - N\Phi/\Phi_0)^2. \quad (10)$$

V_{int} approximates the ground-state energy of the few-particle system and takes different values for different many-body wave functions.

The numerically determined coefficient C_R is essentially a constant (see below). $\Phi = \pi R_{\text{eq}}^2 B$ is the magnetic flux through the ring and $\Phi_0 = h/\eta$ is the magnetic flux quantum. The values of the angular momenta L are not arbitrary. Because of the crystalline symmetries, as well as the symmetric or antisymmetric behavior under particle exchange, they are given by proper sequences of magic angular momenta L_m (see section III A below for further discussion). In particular, all values of angular momenta are allowed for the case of attractive bosons, i.e., $L_m = 0, \pm 1, \pm 2, \dots$. For the case of fully polarized repelling fermions with N odd or spinless repelling bosons with any N , the allowed angular momenta are restricted to the sequence $L_m = kN$, with $k = 0, \pm 1, \pm 2, \dots$. For the case of fully polarized repelling fermions with N even, the allowed angular momenta are given by a different sequence $L_m = (k + 1/2)N$, with $k = 0, \pm 1, \pm 2, \dots$

Due to the very large values of R_W and R_δ , the value of C_R is very close to that of a classical rigid rotor, corresponding to N point particles in their equilibrium configuration inside the annular confinement, i.e., $C_R \approx C_R^{\text{cl}} = \hbar^2/[2\mathcal{I}(R_{\text{eq}})]$, with inertia moment $\mathcal{I}(R_{\text{eq}}) = NMR_{\text{eq}}^2$. As typical examples, in Table I, Table II, and Table III of Appendix A, we list calculated energies according to Eq. (6) for an odd number $N = 7$ and an even number $N = 8$ of fermionic ions, as well as for $N = 10$ attractive bosons, respectively; $R_W = 1000$ for the repelling ions and $R_\delta = 50$ for the attractive bosons. The ratio $\tilde{f} \equiv C_R/C_R^{\text{cl}} \approx 1$ for all $L < 165$ for ions, and for all $L \leq 30$ for attractive bosons. As aforementioned, the rigid-rotor-type spectrum in Eq. (10) was explored earlier in the QSTC literature [13, 35]; however, by itself it does not lead to the derivation of appropriate QSTC wave functions. The demonstrated agreement between the microscopically calculated rotational part of the spectrum [Eq. (6)] and the analytic second term in Eq. (10) expected for a QSTC [13, 35] validates the expressions Φ_L^{PROJ} introduced in Eq. (5) as proper trial wave functions for the QSTC.

We showed previously that the limit of a quantum rigid rotor for a system of strongly interacting particles can also be reached in external confinements with geometries other than the ring geometry. In particular, the rigid-rotor limit for $R_W = 200$ and in a fully two-dimensional parabolic confinement was demonstrated for two electrons in Ref. [66] using exact many-body wave functions and for a few electrons in Ref. [40] using the same ansatz as in Eq. (5) here. In this universal rigid-rotor limit, the rotational part of the spectra is natu-

rally similar. However, the presence of strong many-body correlations (which result from the beyond-mean-field, multi-determinant, or multi-permanent, nature of the wave function) is reflected in the actual numerical values of the first term, V_{int} , in Eq. (10).

In our scheme, which allows for an expanded variational freedom by employing unrestricted orbitals at the mean-field single-determinant, or single-permanent, level (i.e., a different orbital for each particle), the ground-state energy is lowered at every step (see in particular Fig. 1 in Ref. [29]): restricted HF (symmetry conserving) \rightarrow unrestricted HF (symmetry breaking) \rightarrow symmetry restoration via projection techniques (an example of the full scheme can be seen in Fig. 5 of Ref. [29]). This scheme for repelling bosons translates as: symmetry-conserving Gross-Pitaevskii \rightarrow symmetry-breaking ansatz of unrestricted permanent \rightarrow symmetry restoration via projection techniques. We note that allowing the single orbital of the Gross-Pitaevskii equation to break the azimuthal symmetry of the ring leads [67–69] to higher-energy solitonic Bose-Einstein condensate branches in the rotational part of the spectrum, which are sharply different from the QSTC wave functions introduced in this paper.

As a specific example of the lowering of the ground-state energy in our scheme, we report that the energy for the unrestricted ansatz determinant [see Eq. (9)] in the case of $N = 8$ ultracold ions on a ring of radius $R = 200l_0$ with $R_W = 1000$ (case described in Table II of Appendix A) is $E_{\text{UHF}} = 118.1771 \hbar\omega_0$, while the corresponding restored-symmetry ground state has indeed a lower energy $V_{\text{int}} = 117.9271 \hbar\omega_0$. This lowering of the total energy is immense compared to the quantum of the rotational motion $C_R^{\text{cl}} = 1.5614 \times 10^{-6} \hbar\omega_0$ (see caption of TABLE II in Appendix A).

An illustrative case of the rigid-rotor rotational spectra encoded in the second term in Eq. (10) is displayed in Fig. 1. A main feature of these spectra are the crossing points (several of them encircled) between pairs of curves with different L_m 's. The crossings define special magnetic-field values, $\Phi/\Phi_0 = (L_1 + L_2)/(2N)$, in the neighborhood of which the system is particularly susceptible to symmetry breaking via the intermixing of two angular momenta and the ensuing generation of the PWM wave packets [see Eq. (1)].

Because the symmetry-restored (projected) wave function Φ_L^{PROJ} [Eq. (5)] preserves the group-theoretical requirements of the continuous 2D rotational group, its single-particle density is azimuthally uniform. However, the crystalline order of the original MF (symmetry-broken) wave function Ψ^{SB} is not destroyed in the symmetry-restoration step; instead, it mutates into a hidden order, which however can be revealed via the conditional probability distribution (CPD) (density-density correlation function). The CPD is given by

$$\mathcal{D}(\mathbf{r}, \mathbf{r}_0) = \langle \Phi_L^{\text{PROJ}} | \sum_{i \neq j} \delta(\mathbf{r}_i, \mathbf{r}) \delta(\mathbf{r}_j, \mathbf{r}_0) | \Phi_L^{\text{PROJ}} \rangle. \quad (11)$$

The CPD provides the probability of finding a particle in

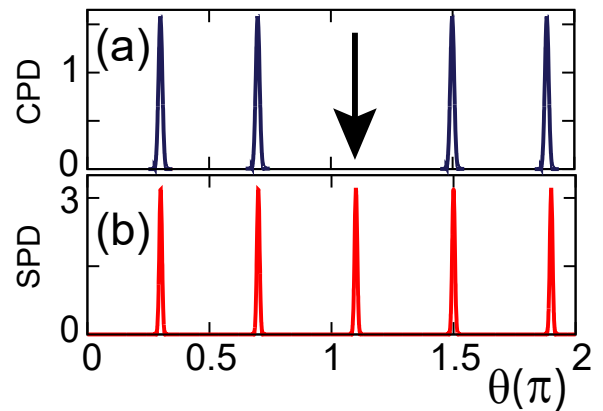


FIG. 2. (a) CPD of the symmetry-restored stationary (beyond MF) state Φ_L^{PROJ} for $N = 5$ fermionic ions along the perimeter of the ring (at a radius R_{eq}). The arrow at $\theta_0 = 1.1\pi$ denotes the fixed point $\mathbf{r}_0 = R_{\text{eq}}e^{i\theta_0} = R_{\text{eq}}e^{1.1i\pi}$. Note the $2\pi/5$ angle between the nearest-neighbor humps and between the arrow and the two adjacent humps. Other parameters are: magic angular momentum $L = L_m = N$, $R_W = 200$, $R = 40l_0$, $l_0 = 50$ nm, and $\Phi/\Phi_0 = 0.8$. There is no hump at the fixed point. CPD in units of $10^{-2}/(2\pi\lambda^4)$. (b) SPD of the original MF state $\Psi^{\text{SB}}(\gamma = 0.1\pi)$ (a determinant) for $N = 5$ fermionic ions, exhibiting explicitly symmetry breaking. Other parameters are $R = 40l_0$, $l_0 = 50$ nm. SPD in units of $10^{-1}/(2\pi\lambda^2)$. In contrast to the symmetry-broken MF SPD in (b), the SPD of the symmetry-restored, beyond-mean-field Φ_L^{PROJ} is azimuthally uniform; see black dashed line in Fig. 3(a). Azimuthal angle θ in units of π .

position \mathbf{r} assuming that another one is located at the fixed point \mathbf{r}_0 . Substitution of the expression [Eq. (5)] that defines Φ_L^{PROJ} , yields for $\mathcal{D}(\mathbf{r}, \mathbf{r}_0)$ a double integral over the azimuthal angles γ_1 and γ_2 ; this integral expression is given in the Appendix B.

Fig. 2(a) displays an illustrative example of the hidden order in the symmetry-restored wave function Φ_L^{PROJ} . The CPD in Fig. 2(a) exhibits well localized features; it contrasts with the uniform horizontal black dashed lines in Figs. 3(a) and 3(b) which describe $\rho(\mathbf{r}, t)$'s of Φ_L^{PROJ} along the perimeter of the ring trap (at a radius R_{eq}). We stress that the fixed point \mathbf{r}_0 in the CPD is arbitrary, i.e., the four peaks in the CPD in Fig. 2(a) readjust to a different choice of θ_0 so that the relative distance between them and the arrow remain unchanged. Fig. 2(b) displays the SPD of the original state $\Psi^{\text{SB}}(\gamma = 0.1\pi)$ (a determinant) for $N = 5$ fermionic ions, exhibiting explicitly the symmetry breaking at the mean-field level.

C. Third level (beyond mean field): Periodic time evolution of the spatially inhomogeneous $\rho(\mathbf{r}, t)$ associated with the wavepacket $\Phi^{\text{PWM}}(L_1, L_2; t = 0)$

As aforementioned, the two-state wave packet in Eq. (1) is not an eigenstate of the total angular momentum, and thus it is not a stationary state when the pinning

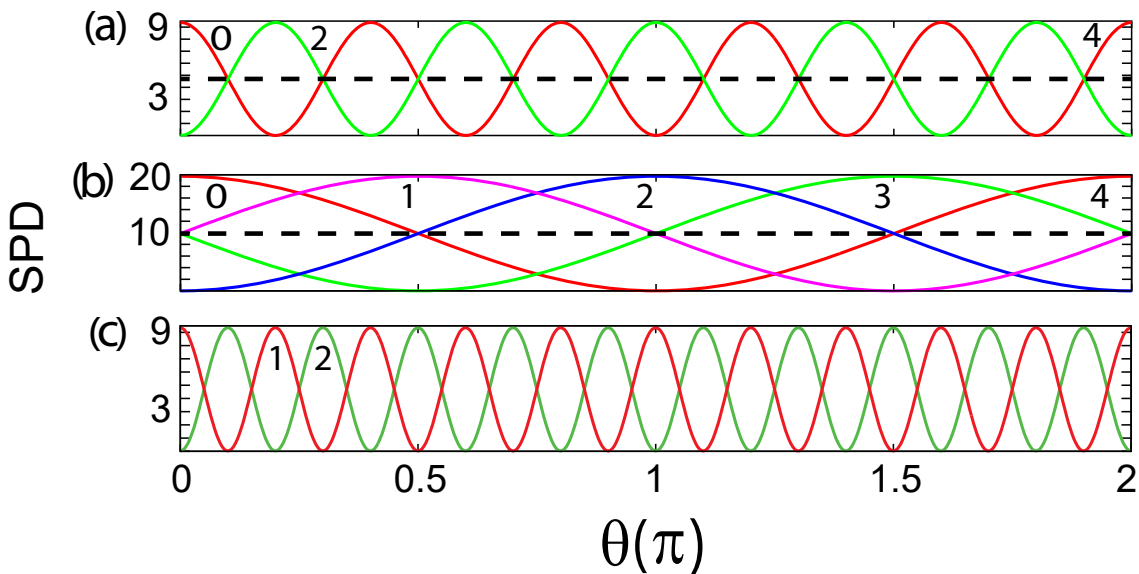


FIG. 3. Snapshots of undamped inhomogeneous single-particle densities rotating around the ring that were calculated with the wave packet $\Phi^{\text{PWM}}(L_1, L_2; t)$. (a) $N = 5$ fermionic ions and magic angular momenta $L_1 = 0$, $L_2 = N$. The SPDs are shown for the time instances $t_j = j\tau/4$, with $j = 0$, $j = 2$, and $j = 4$ (the j 's label the curves); $\tau = 2\pi\hbar/(|E^{\text{PROJ}}(L_2) - E^{\text{PROJ}}(L_1)|)$. Other parameters: $\alpha = \beta = 1/\sqrt{2}$, $R_W = 200$, $R = 60l_0$, $l_0 = 50$ nm, and $\Phi/\Phi_0 = 1.8$. (b) $N = 7$ attractive bosons and magic angular momenta $L_1 = 0$, $L_2 = 1$. The SPDs are shown for the time instances $t_j = j\tau/4$, $j = 0, 1, \dots, 4$. Other parameters: $\alpha = \beta = 1/\sqrt{2}$, $R_\delta = 50$, $R = 40l_0$, $l_0 = 1$ μm , and $\Phi/\Phi_0 = 6.4$. The black horizontal dashed lines represent the uniform density of either one of the stationary states $\Phi_{L_m}^{\text{PROJ}}$ (with $L_m = L_1$ or $L_m = L_2$) that contribute to the nonstationary wave packet $\Phi^{\text{PWM}}(L_1, L_2; t)$. (c) $N = 5$ fermionic ions and magic angular momenta $L_1 = 0$, $L_2 = 2N$ (higher-harmonic of the QSTC). $t_j = j\tau/4$, with $j = 1$ and $j = 2$. Other parameters as in (a). For repelling ions, panels (a) and (c), the period is $T = \tau/N$; for attractive bosons, the period is $T = \tau$. The SPDs are in units of $10^{-2}/(2\pi\lambda^2)$. Azimuthal angle θ in units of π .

agent is lifted; such a pinning agent could be implemented, for example, as a distortion of the circular geometry of the trap confinement, or as a modulation of the trap potential in the azimuthal direction along the ring [6]. (A sudden variation of the magnetic field can also transform an eigenstate $\Phi_L^{\text{PROJ}}(B_1)$ at a given B_1 value to a superposition of $\Phi_L^{\text{PROJ}}(B_2)$ states at another B_2 value [65].) The resulting time evolution is associated with a time-dependent phase $\phi(t)$ as discussed previously. Here we will show explicitly that $\phi(t)$ represents an undamped rotation of spatially inhomogeneous $\rho(\mathbf{r}, t)$'s around the ring, so that the many-body $\Phi^{\text{PWM}}(L_1, L_2; t)$ exhibit the desired behavior of a QSTC. The successful theoretical identification and experimentally implemented superposition of two appropriate many-body spin eigenstates of the Ising Hamiltonian (resulting in a “spin Schrödinger-Cat” state) were keys to the emulation of the “weaker class” of discrete time crystals [21, 22, 24, 26].

The $\rho(\mathbf{r}, t)$ of $\Phi^{\text{PWM}}(L_1, L_2; t)$ is defined as

$$\rho(\mathbf{r}; t) = \langle \Phi^{\text{PWM}}(L_1, L_2; t) | \sum_{i=1}^N \delta(\mathbf{r}_i - \mathbf{r}) | \Phi^{\text{PWM}}(L_1, L_2; t) \rangle. \quad (12)$$

As in the case of the CPD, $\rho(\mathbf{r}; t)$ entails a double integral over the azimuthal angles γ_1 and γ_2 ; the lengthy expression is given in Appendix C.

Fig. 3 displays the periodic time evolution of $\rho(\mathbf{r}, t)$'s for two illustrative $\Phi^{\text{PWM}}(L_1, L_2; t)$ cases, one for $N = 5$ Coulomb repelling fermionic ions [Fig. 3(a)] with $L_2 - L_1 = N$ and the other for $N = 7$ neutral bosons with $L_2 - L_1 = 1$ [Fig. 3(b)] interacting via an attractive contact interaction. The $\rho(\mathbf{r}, t)$'s were calculated at times $t_j = j\tau/4$, where $\tau = 2\pi\hbar/(|E^{\text{PROJ}}(L_2) - E^{\text{PROJ}}(L_1)|)$; the actual used j 's label the $\rho(\mathbf{r}, t)$ curves. The number of humps exhibited by the PWM $\rho(\mathbf{r}, t)$'s in Fig. 3(a) and Fig. 3(b) is equal to that in the original MF densities, i.e., N for the repelling-fermions PWM and one for the attractive-bosons lump. The period of the PWM $\rho(\mathbf{r}, t)$'s is $T = \tau/N$ for repelling ions and $T = \tau$ for attractive bosons.

Finally, Fig. 3(c) demonstrates a different state of matter, i.e., multi-harmonic excitations of the QSTC exhibiting a multiple number of density humps, i.e., kN and k (with $k = 2, 3, \dots$), corresponding to $\Phi^{\text{PWM}}(L_1, L_2; t)$'s with $L_2 - L_1 = kN$ for repelling fermions and with $L_2 - L_1 = k$ for attractive bosons, respectively.

We note that the PWM broken-symmetry state introduced here to describe a QSTC has an energy intermediate between E_1 and E_2 because $\alpha^2 + \beta^2 = 1$ (i.e., $E^{\text{PWM}} = \alpha^2 E_1 + \beta^2 E_2$). In particular, at the crossing point of the two parabolas (where $E_1 = E_2 = E_{\text{cross}}$), one has always $E^{\text{PWM}} = E_{\text{cross}}$. This contrasts with the behavior of the energy of the non-crystalline states studied

in Refs. [67–69], which lies always well above the crossing point.

III. DISCUSSION

A. Symmetries of the trial wave functions, magic angular momenta, and rigidity

Despite the fact that the trial wave functions in Eq. (5) are a good approximation to the rotational-symmetry-preserving many-body eigenstates, they do embody and reflect in an optimum way the crystalline point-group symmetries (familiar from bulk crystals). Specifically, the C_N point-group symmetry of the “classical” crystal, which is accounted for through the kernel of symmetry-broken MF determinants (or permanents) Ψ^{SB} , is reflected in the fact that the trial wave functions Φ_L^{PROJ} are identically zero except for a subset of *magic* angular momenta L_m .

In the case of N repelling particles, the magic total angular momenta can be determined by considering the point-group symmetry operator $\hat{R}(2\pi/N) \equiv \exp(-i2\pi\hat{L}/N)$ that rotates on the ring simultaneously the localized particles by an angle $2\pi/N$. In connection to the state Φ_L^{PROJ} , the operator $\hat{R}(2\pi/N)$ can be invoked in two different ways, namely either by applying it on the “intrinsic” part Ψ^{SB} or the “external” phase factor $\exp(i\gamma L)$ (see Ch. 4-2c Ref. [70]). One gets in the case of fermions

$$\hat{R}(2\pi/N)\Phi_L^{\text{PROJ}} = (-1)^{N-1}\Phi_L^{\text{PROJ}}, \quad (13)$$

from the first alternative and

$$\hat{R}(2\pi/N)\Phi_L^{\text{PROJ}} = \exp(-2\pi Li/N)\Phi_L^{\text{PROJ}}, \quad (14)$$

from the second alternative. The $(-1)^{N-1}$ factor in Eq. (13) results from the fact that the $2\pi/N$ rotation is equivalent to exchanging $N-1$ rows in the Ψ^{SB} determinant. Now if $\Phi_L^{\text{PROJ}} \neq 0$, the only way that Eqs. (13) and (14) can be simultaneously true is if the condition $\exp(2\pi Li/N) = (-1)^{N-1}$ is fulfilled. This leads to the following sequence of magic angular momenta,

$$L_m = kN; \quad k = 0, \pm 1, \pm 2, \pm 3, \dots, \quad (15)$$

for N odd, and

$$L_m = (k + \frac{1}{2})N; \quad k = 0, \pm 1, \pm 2, \pm 3, \dots, \quad (16)$$

for N even.

Because a permanent is symmetric under the interchange of two rows, the corresponding magic L_m 's for spinless bosons are given by the sequence in Eq. (15) for both odd and even numbers of localized bosons.

Regarding the numerical aspects, the fact that Φ_L^{PROJ} is zero for non-magic L values results in the vanishing (within machine precision) of the normalization factor

$\int_0^{2\pi} n(\gamma)e^{i\gamma L}d\gamma$ in Eq. (6). As a result only the physically meaningful energies associated with magic angular momenta are given in Table I, Table II, and Table III of Appendix A.

We stress that the properties and physics associated with magic-angular-momentum yrast states are well known in the literature of 2D quantum dots [29, 71–74]. Of immediate relevance to this paper is the enhanced energy stabilization that they acquire in their neighborhood (thus characterized often as “cusp” states) in the regime of strong interactions (i.e., for large R_W or R_δ). This energy stabilization can be explicitly seen in Fig. 15 of Ref. [29], where the triplet state corresponds to the fully polarized case for two electrons with magic angular momenta $L_m = (2k+1)$, $k = 0, \pm 1, \pm 2, \dots$. The fact that large energy gaps do develop between the magic-angular-momentum rotational yrast states and the other (excited) states is also well established in the QSTC literature; for the case of ultracold ions on a ring, see Refs. [13, 35], and for the case of the bosonic lump, see Ref. [12].

In this paper, we consider fully polarized fermions only, that is cases when $S = S_z = N/2$, where S is the total spin and S_z is its projection. Consideration with our methodology of the other spin values $S_z < N/2$ is straightforward; it requires, however, restoration of both the total spin \mathbf{S}^2 and the total angular momentum. An explicit example for $N = 3$ fermions is discussed in Ref. [39].

In addition to the magic angular momenta, the properties of the original crystalline structure built-in in Ψ^{SB} are reflected in the high-degree of rigidity exhibited by the symmetry-preserving Φ_L^{PROJ} . As demonstrated previously, the SPD of Φ_L^{PROJ} is uniform, but the CPD of Φ_L^{PROJ} reveals the now hidden crystalline structure of N strongly repelling particles on the ring. The rigidity of Φ_L^{PROJ} is manifested in that the CPDs have the same N -hump shape and are independent of the actual value of the magic angular momenta, as well as of the fermion or boson statistics and of whether the number N of fermions is odd or even. This rigidity is a consequence of the strong two-body interaction and cannot be found in many-body wave functions associated with weak interparticle interactions.

B. Initial wave packets and associated time evolution

The focus of this paper is the construction of a symmetry-preserving wave function Φ_L^{PROJ} associated with the finite-crystal symmetry-broken determinant (or permanent) Ψ^{SB} . However, it is instructive to inquire about the reverse process, that is how to represent the symmetry-broken crystal as a superposition in the complete basis formed by the symmetry-preserving Φ_L^{PROJ} 's.

Indeed one can write the expansion

$$\Psi^{\text{SB}} = \sum_L \mathcal{C}_L \Phi_L^{\text{PROJ}}, \quad (17)$$

where [using Eq. (5)] the expansion coefficients are given by

$$\mathcal{C}_L = \frac{1}{2\pi} \int_0^{2\pi} d\gamma e^{-i\gamma L} n(\gamma), \quad (18)$$

and the norm overlap $n(\gamma)$ was defined in Eq. (8). Of course the index L runs over the appropriate sequence of magic angular momenta as discussed in Section III A.

Eqs. (17) and (18) illustrate the fact that with respect to the exact many-body (linear) Schrödinger equation the symmetry-broken-crystal wave function Ψ^{SB} is a wave packet and not a stationary eigenstate. This is also in general true for all SB mean-field solutions, whether they are solutions of the unrestricted Hartree-Fock equations in the case of confined electrons (e.g., in quantum dots [29]), or they are the familiar solitonic solutions of the Gross-Pitaevskii equations in onedimensional bosonic systems. Due to the rapid experimental control, the latter cases are currently attracting a lot of attention. Indeed motivated by experiments that suggest the need to go beyond-mean field dynamics, the number of related theoretical investigations has burgeoned [30–34].

These theoretical studies investigate how an initial state approximating a solution of the nonlinear Gross-Pitaevskii equation evolves in time under the exact many-body Hamiltonian. For both the cases of dark [30, 31] (a hole in matter density) and bright [32–34] solitons (an excess in matter density, like the case of the hump considered in this paper), these studies are finding a “universal” behavior of dispersion in space, decay in time, and time revival at the initial position of the soliton. This behavior can be understood by taking into consideration the expansion in Eq. (17). In fact, each energy mode in Eq. (17) will evolve in time according to its own phase $\exp(-iE_L t/\hbar)$, and the interaction between all of them results in a decay-type behavior. Moreover, the initial occupation amplitudes \mathcal{C}_L^2 of the different modes are unequal, and as a result probability flows from the higher occupied modes to those with lower initial occupations, which leads to a dispersive behavior. However, because the system is finite, there exists a Poincaré period, and the system will eventually experience a revival [75, 76].

For achieving a QSTC, we propose here a different initial wave packet, i.e., a two-mode one with equal weights, as specified in Eq. (1). As explicitly demonstrated through numerical calculations, such a two-mode initial wave packet preserves at all times, and without damping, the spatial and temporal periodicities expected from the classical finite crystal. We note that the consideration of two-mode Schrödinger-cat states is a key element in the theory of the discrete time crystal, where the focus is to enable a sloshing behavior between these specialized paired states by minimizing interactions to the

rest of the system. In fact, our symmetry-preserving trial functions Φ_L^{PROJ} [see Eq. (5)] can be viewed as a more complex class of Schrödinger-cat states. This analogy is straightforward for the case of the mirror superposition used in Ref. [20], which can be reproduced from expression (5) as a limiting case by using only two angles $\gamma_1 = 0$ and $\gamma_2 = \pi$.

C. Relation to configuration-interaction (CI) wave functions

As mentioned previously, the symmetry-preserving trial functions Φ_L^{PROJ} are identically zero for values of L different from the magic angular momenta L_m ; see section III A. Naturally the exact many-body spectrum has a plethora of additional states with good L , which however cannot be reached with the approach in this paper. Indeed this approach is tuned to extracting from the complete spectrum only the ground states that correspond to non-vibrating classical finite crystal arrangements. The remaining many-body states can be reached by using the CI approach, which is in principle an exact methodology when converged; the CI is often referred to as exact diagonalization (EXD). The CI approach is computationally expensive, but comparisons between the symmetry-restored trial functions and the CI wave functions have been used by us to demonstrate the numerical accuracy of the symmetry-restored wave functions, as well as to clarify their special place in the whole spectrum, namely that for particular magnetic-field ranges they can become the global ground state, as is the case with the Aharonov-Bohm spectrum in Fig. 1 of the present paper. Higher-in-energy CI solutions with different L (and also with $L = L_m$) do incorporate vibrational and other type of internal excitations, and as a result a superposition of two random CI states with good L_1 and L_2 will not necessarily exhibit the crystalline single-particle-density structure of exactly N humps.

Systematic comparisons between symmetry-restored states and CI wave functions have been carried out by us previously for the case of a few electrons confined in parabolic quantum dots. Although the external confining potential and particle species in parabolic QDs are different from the case of the ring traps considered here, the symmetry properties of the many-body wave functions are universal. Thus the analysis presented in our previous QD studies can be used to gain further insights to the results for the QSTC presented in section II. In particular, Fig. 6 and Fig. 7 of Ref. [44] offer an explicit illustration of the fact that N -humped crystalline SPD structures arise only when both L_1 and L_2 coincide with magic angular momenta and the associated CI wave functions correspond to global ground states in some range of magnetic fields (see Fig. 5 and section III in Ref. [44]).

In our previous studies of QDs, excellent agreement was found between the total energies of symmetry-restored trial functions and the corresponding CI energies

for both the cases with or without an applied magnetic field, as testified by the many reported direct numerical comparisons. We mention here a few specific examples, i.e., Table III and IV in Ref. [39], Table IV in Ref. [38], and Fig. 4 in Ref. [43].

Such systematic numerical comparisons between symmetry-restored and CI wave functions for the case of ring-trapped ultracold ions and neutral bosons are outside the scope of the present paper. However, they will be reported in subsequent publications [65], including the case away from the quasi-1D regime (when the dependence on the ring width becomes important).

IV. CONCLUSIONS

The discussion [17–19], motivated by the criticism [14–16, 19] of the original [12, 13] QSTC proposals (which were based on ground states), spurred speculations about non-equilibrium low-lying states as possible instruments for describing QSTCs. For N rotating particles on a ring, and using the theory of symmetry breaking and symmetry restoration via projection techniques [29], this paper succeeded in explicitly uncovering the existence of low-lying states with QSTC behavior, by introducing beyond-MF appropriate trial many-body wave functions (see Fig. 3). Along with its conceptual and methodological significance, we propose to focus experimental attention on selected applied magnetic field values where the Aharonov-Bohm-type spectra corresponding to different magic angular momenta are most susceptible to mixing (Fig. 1), resulting in rotating pinned-Wigner-molecule many-body states found here to exhibit QSTC behavior. This constructive platform fills an apparent gap in the quest for ultracold ring-confined ions or neutral-atom QSTCs.

We recall that although the original proposals for the quantum space-time crystal [12, 13] suggested realization of the concept through the use of ultracold few ring-trapped particles, this is yet to be achieved experimentally. Nevertheless, for the case of ultracold ions, several publications have reported significant progress in controlling aspects of a quantum rotor on a ring. In particular, the ability to generate and control symmetry-breaking through pinning of the rotating ion crystal has been demonstrated by using up to 15 $^{40}\text{Ca}^+$ ions in a ring with a microfabricated silicon surface Paul trap [6], or 3 $^{40}\text{Ca}^+$ ions in a 2D ring-type configuration in a lin-

ear Paul trap [7]. To fully implement and control the QSTC trial functions presented in this paper, the ions need to be cooled down to near the ground states. In this respect, Ref. [6] has achieved temperatures ~ 3 mK (for a trap with a radius of ~ 60 μm), while Ref. [7] reported temperatures in the nanometer range (for an effective ring radius in the 6 to 8 micrometer range). It is expected that cooling techniques and procedures will be further optimized and will be successful in the near future in producing near-ground-state temperatures, as is exemplified by a very recent publication [77].

An essential requirement, met by our theory, is that it is imperative that the proposed beyond-mean-field many-body trial wave functions (i.e., beyond the UHF or GP treatments) for predicting proper quantum space-time-crystal behavior of particles moving on a ring will be based on solutions to the interacting particles Schrödinger equation that possess good angular momenta, as well as exhibit (hidden) ordering that reflects an underlying finite crystalline symmetry. This is achieved in our theory through the first two construction stages, namely, the unrestricted Hartree-Fock solution followed by an angular momentum projection, yielding the function Φ_L^{PROJ} [Eq. (5)]. It is then proposed by us that these projected and stationary many-body wave functions are susceptible to mixing, see Eq. (1), favored to occur in the vicinity of crossings of Aharonov-Bohm-type spectra of ground-state energies *vs.* applied magnetic field (see circles in Fig. 1). This mixing results in non-stationary low-lying states that, when evolved with the many-body Hamiltonian, yield undamped and non-dispersing periodic oscillations in both space and time.

ACKNOWLEDGMENTS

Work supported by the Air Force Office of Scientific Research under Award No. FA9550-15-1-0519. Calculations were carried out at the GATECH Center for Computational Materials Science.

Appendix A: Numerical Calculations of the many-body rotational energies $E^{\text{PROJ}}(L_m)$ [Eq. (6)]

Tables I, II, and III below present three illustrative examples of the rotational energy spectra $E^{\text{PROJ}}(L_m)$ according to numerical calculations of the many-body expression in Eq. (6) of the main text. The captions explain how the numerical C_R in Eq. (10) is extracted from the computed values of $E^{\text{PROJ}}(L_m)$. C_R is found to be very close to the classical rigid-rotor value $C_R^{\text{cl}} = \hbar^2/[2\mathcal{I}(R_{\text{eq}})]$.

TABLE I. Rotational energy spectra according to Eq. (6) and ratio $\tilde{f} \equiv C_R/C_R^{\text{cl}}$ for $N = 7$ spin polarized ultracold fermionic ions at two different magnetic fields $\Phi = 0$ and $\Phi/\Phi_0 = 3.2$. The interparticle interaction is a repelling Coulomb potential. The energies are in units of $\hbar\omega_0 = \hbar^2/(Ml_0^2)$. The remaining parameters are: Wigner parameter $R_W = 1000$, ring radius $R = 200l_0$, and oscillator strength $l_0 = 50$ nm. As a function of L_m , the numerically extracted coefficient C_R in Eq. (10) was determined from the ratio $C_R = (E^{\text{PROJ}}(L_m) - E^{\text{PROJ}}(L_m - N)) / (N(2L_m - 2\Phi N/\Phi_0 - N))$. Its value is practically constant and equal to C_R^{cl} ; see the values of the ratio \tilde{f} , which are very close to unity. The classical rigid-body value is $C_R^{\text{cl}} = 1.7847 \times 10^{-6} \hbar\omega_0$. The underlined numbers refer to the ground state for a given Φ/Φ_0 .

$N = 7$ fermions, $\Phi = 0$			$N = 7$ fermions, $\Phi/\Phi_0 = 3.2$		
L_m	$E^{\text{PROJ}}(L_m)$	\tilde{f}	L_m	$E^{\text{PROJ}}(L_m)$	\tilde{f}
<u>0</u>	<u>85.6564962006</u>		0	85.6573927150	
7	85.6565836512	1.000011	7	85.6569201655	1.000681
14	85.6568460029	1.000011	14	85.6566225173	1.001074
21	85.6572832557	1.000011	<u>21</u>	<u>85.6564997702</u>	1.002594
28	85.6578954097	1.000011	28	85.6565519241	0.993980
35	85.6586824648	1.000011	35	85.6567789793	0.998619
...
105	85.6761725766	1.000011	105	85.6686690913	0.999850
112	85.6788835437	1.000010	112	85.6708200583	0.999863
119	85.6817694118	1.000010	119	85.6731459265	0.999874
126	85.6848301808	1.000010	126	85.6756466955	0.999884
133	85.6880658508	1.000010	133	85.6783223655	0.999892
140	85.6914764217	1.000010	140	85.6811729366	0.999899

TABLE II. Rotational energy spectra according to Eq. (6) and ratio $\tilde{f} \equiv C_R/C_R^{\text{cl}}$ for $N = 8$ spin polarized ultracold fermionic ions at two different magnetic fields $\Phi = 0$ and $\Phi/\Phi_0 = 3.2$. The interparticle interaction is a repelling Coulomb potential. The energies are in units of $\hbar\omega_0 = \hbar^2/(Ml_0^2)$. The remaining parameters are: Wigner parameter $R_W = 1000$, ring radius $R = 200l_0$, and oscillator strength $l_0 = 50$ nm. As a function of L_m , the numerically extracted coefficient C_R in Eq. (10) was determined from the ratio $C_R = (E^{\text{PROJ}}(L_m) - E^{\text{PROJ}}(L_m - N)) / (N(2L_m - 2\Phi N/\Phi_0 - N))$. Its value is practically constant and equal to C_R^{cl} ; see the values of the ratio \tilde{f} , which are very close to unity. The classical rigid-body value is $C_R^{\text{cl}} = 1.5614 \times 10^{-6} \hbar\omega_0$. The underlined numbers refer to the ground state for a given Φ/Φ_0 .

$N = 8$ fermions, $\Phi = 0$			$N = 8$ fermions, $\Phi/\Phi_0 = 3.2$		
L_m	$E^{\text{PROJ}}(L_m)$	\tilde{f}	L_m	$E^{\text{PROJ}}(L_m)$	\tilde{f}
<u>4</u>	<u>117.9270981536</u>		4	117.9278028694	
12	117.9272980155	1.000010	12	117.9273627314	1.001015
20	117.9276977394	1.000010	20	117.9271224553	1.001852
28	117.9282973253	1.000010	<u>28</u>	<u>117.9270820410</u>	1.011065
36	117.9290967731	1.000010	36	117.9272414889	0.997248
44	117.9300960828	1.000010	44	117.9276007987	0.998782
...
124	117.9510815852	1.000010	124	117.9421863015	0.999823
132	117.9542793756	1.000010	132	117.9447440920	0.999837
140	117.9576770279	1.000010	140	117.9475017443	0.999850
148	117.9612745420	1.000010	148	117.9504592585	0.999860
156	117.9650719179	1.000010	156	117.9536166343	0.999870
164	117.9690691554	1.000010	164	117.9569738719	0.999878

TABLE III. Rotational energy spectra according to Eq. (6) and ratio $\tilde{f} \equiv C_R/C_R^{\text{cl}}$ for $N = 10$ spinless ultracold bosons at two different magnetic fields $\Phi = 0$ and $\Phi/\Phi_0 = 2.464$. The interparticle contact interaction is attractive. The energies are in units of $\hbar\omega_0 = \hbar^2/(Ml_0^2)$. The remaining parameters are: Wigner parameter $R_\delta = 50$, ring radius $R = 40l_0$, and oscillator strength $l_0 = 1 \mu\text{m}$. As a function of L_m , the numerically extracted coefficient C_R in Eq. (10) was determined from the ratio $C_R = (E^{\text{PROJ}}(L_m) - E^{\text{PROJ}}(L_m - 1)) / (2L_m - 2\Phi N/\Phi_0 - 1)$. Its value is practically constant and equal to C_R^{cl} ; see the values of the ratio \tilde{f} , which are very close to unity. The classical rigid-body value is $C_R^{\text{cl}} = 3.1250 \times 10^{-5} \hbar\omega_0$. The underlined numbers refer to the ground state for a given Φ/Φ_0 .

$N = 10$ bosons, $\Phi = 0$			$N = 10$ bosons, $\Phi/\Phi_0 = 2.464$		
L_m	$E^{\text{PROJ}}(L_m)$	\tilde{f}	L_m	$E^{\text{PROJ}}(L_m)$	\tilde{f}
<u>0</u>	<u>-350.8488583900</u>		<u>0</u>	<u>-350.8303108498</u>	
1	-350.8488271326	1.000234	1	-350.8318195924	0.999995
2	-350.8487333607	1.000234	2	-350.8332658201	0.999985
3	-350.8485770740	1.000234	3	-350.8346495329	0.999973
4	-350.8483582728	1.000234	4	-350.8359707308	0.999961
5	-350.8480769568	1.000234	5	-350.8372294139	0.999947
...
23	-350.8323232897	1.000231	23	-350.8491956906	0.997529
24	-350.8308542000	1.000231	24	-350.8492665957	0.995160
25	-350.8293225964	1.000231	<u>25</u>	<u>-350.8492749867</u>	0.958962
26	-350.8277284788	1.000231	26	-350.8492208634	1.006945
27	-350.8260718473	1.000230	27	-350.8491042260	1.003333
28	-350.8243527019	1.000230	28	-350.8489250745	1.002246
29	-350.8225710428	1.000230	29	-350.8486834090	1.001722
30	-350.8207268699	1.000229	30	-350.8483792296	1.001414

Appendix B: Conditional Probability Distribution

The explicit expression for the CPDs of the symmetry-restored wave functions Φ_L^{PROJ} [see Eq. (11)] is given by

$$\mathcal{D}(\mathbf{r}, \mathbf{r}_0) = \frac{\int_0^{2\pi} d\gamma_1 \int_0^{2\pi} d\gamma_2 e^{i(\gamma_1 - \gamma_2)L} \sum_{k \neq m, l \neq n} (\mathcal{G}_{km}^{ln}(\gamma_1, \gamma_2) \mp \mathcal{G}_{km}^{nl}(\gamma_1, \gamma_2)) \mathcal{S}_{ln}^{km}(\gamma_1, \gamma_2)}{2\pi \int_0^{2\pi} n(\gamma) e^{i\gamma L} d\gamma}, \quad (\text{A.1})$$

where

$$\mathcal{G}_{km}^{ln}(\gamma_1, \gamma_2) = \frac{1}{\pi^2 \lambda^4} \exp \left(- \frac{(\mathbf{r} - \mathbf{R}_k(\gamma_1))^2 + (\mathbf{r} - \mathbf{R}_l(\gamma_2))^2 + (\mathbf{r}_0 - \mathbf{R}_m(\gamma_1))^2 + (\mathbf{r}_0 - \mathbf{R}_n(\gamma_2))^2}{2\lambda^2} \right) \times \exp \left(\frac{i(x(Y_k(\gamma_1) - Y_l(\gamma_2)) + y(X_l(\gamma_2) - X_k(\gamma_1)) + x_0(Y_m(\gamma_1) - Y_n(\gamma_2)) + y_0(X_n(\gamma_2) - X_m(\gamma_1)))}{2l_B^2} \right), \quad (\text{A.2})$$

and the $\mathcal{S}_{ln}^{km}(\gamma_1, \gamma_2)$'s are two-row (km)-two-column (ln) cofactors of the determinant (minors of the permanent) constructed out of the overlaps of the localized space orbitals $u(\mathbf{r}, \mathbf{R}_j)$ [Eq. (3)]. The \mp sign in Eq. (A.1) corresponds to fermions or bosons.

Appendix C: Single-Particle Density

The explicit expression for the SPDs of the broken-symmetry wave packets $\Phi^{\text{PIN}}(L_1, L_2; t)$ [see Eq. (12)] is given by

$$\rho(\mathbf{r}; t) = \frac{\int_0^{2\pi} d\gamma_1 \int_0^{2\pi} d\gamma_2 (\alpha^2 e^{i(\gamma_1 - \gamma_2)L_1} + \alpha\beta e^{i(\gamma_1 L_1 - \gamma_2 L_2 - \phi(t))} + \alpha\beta e^{i(\gamma_1 L_2 + \phi(t) - \gamma_2 L_1)} + \beta^2 e^{i(\gamma_1 - \gamma_2)L_2}) \sum_{kl} \mathcal{F}_{kl}(\gamma_1, \gamma_2) \mathcal{S}_l^k(\gamma_1, \gamma_2)}{2\pi \int_0^{2\pi} n(\gamma) (\alpha^2 e^{i\gamma L_1} + \beta^2 e^{i\gamma L_2}) d\gamma}, \quad (\text{A.3})$$

where

$$\mathcal{F}_{kl}(\gamma_1, \gamma_2) = \frac{1}{\pi\lambda^2} \exp\left(-\frac{(\mathbf{r} - \mathbf{R}_k(\gamma_1))^2 + (\mathbf{r} - \mathbf{R}_l(\gamma_2))^2}{2\lambda^2}\right) \times \exp\left(-i\frac{y(X_l(\gamma_2) - X_k(\gamma_1)) + x(Y_k(\gamma_1) - Y_l(\gamma_2))}{2l_B^2}\right), \quad (\text{A.4})$$

and the $\mathcal{S}_l^k(\gamma_1, \gamma_2)$'s are one-row (k)-one-column (l) cofactors of the determinant (minors of the permanent) constructed out of the overlaps of the localized space orbitals $u(\mathbf{r}, \mathbf{R}_j)$ [Eq. (3)].

-
- [1] I. Bloch, J. Dalibard, and W. Zwerger, Many-body physics with ultracold gases, *Rev. Mod. Phys.* **80**, 885 (2008).
- [2] R. Blatt and C.F. Roos, Quantum simulations with trapped ions, *Nature Phys.* **8**, 277 (2012),
- [3] N. Goldman, G. Juzeliūnas, P. Öhberg, and I.B. Spielman, Light-induced gauge fields for ultracold atoms, *Rep. Prog. Phys.* **77**, 126401 (2014).
- [4] B. Tabakov, F. Benito, M. Blain, C.R. Clark, S. Clark, R.A. Haltli, P. Maunz, J.D. Sterk, Ch. Tigges, and D. Stick, Assembling a ring-shaped crystal in a microfabricated surface ion trap, *Phys. Rev. Applied* **4**, 031001 (2015).
- [5] P.-J. Wang, T. Li, C. Noel, A. Chuang, X. Zhang, and H. Häffner, Surface traps for freely rotating ion ring crystals, *J. Phys. B: At. Mol. Opt. Phys.* **48**, 205002 (2015).
- [6] H.-K. Li, E. Urban, C. Noel, A. Chuang, Y. Xia, A. Ransford, B. Hemmerling, Y. Wang, T. Li, H. Häffner, and X. Zhang, Realization of translational symmetry in trapped cold ion rings, *Phys. Rev. Lett.* **118**, 053001 (2017).
- [7] A. Noguchi, Y. Shikano, K. Toyoda, and S. Urabe, AharonovBohm effect in the tunnelling of a quantum rotor in a linear Paul trap, *Nat. Commun.* **5**, 3868 (2014).
- [8] C. Ryu, K.C. Henderson, and M.G. Boshier, Creation of matter wave Bessel beams and observation of quantized circulation in a BoseEinstein condensate, *New J. Phys.* **16**, 013046 (2014).
- [9] S. Moulder, S. Beattie, R.P. Smith, N. Tammuz, and Z. Hadzibabic, Quantized supercurrent decay in an annular Bose-Einstein condensate, *Phys. Rev. A* **86**, 013629 (2012).
- [10] A. Ramanathan, K.C. Wright, S.R. Muniz, M. Zeelan, W.T. Hill, III, C.J. Lobb, K. Helmerson, W.D. Phillips, and G.K. Campbell, Superflow in a toroidal Bose-Einstein condensate: An atom circuit with a tunable weak link, *Phys. Rev. Lett.* **106**, 130401 (2011).
- [11] Refs. [4–6, 8–10] describe specifically recent experimental advances in the area of ultracold ring-shaped traps.
- [12] F. Wilczek, Quantum time crystals, *Phys. Rev. Lett.* **109**, 160401 (2012).
- [13] T. Li, Z.-X. Gong, Z.-Q. Yin, H.T. Quan, X. Yin, P. Zhang, L.-M. Duan, and X. Zhang, Space-time crystals of trapped ions, *Phys. Rev. Lett.* **109**, 163001 (2012).
- [14] P. Bruno, Comment on “Quantum Time Crystals”, *Phys. Rev. Lett.* **110**, 118901 (2013); Comment on “Space-Time Crystals of Trapped Ions”, *Phys. Rev. Lett.* **111**, 029301 (2013).
- [15] P. Bruno, Impossibility of spontaneously rotating time crystals: A no-go theorem, *Phys. Rev. Lett.* **111**, 070402 (2013).
- [16] Ph. Nozières, Time crystals: Can diamagnetic currents drive a charge density wave into rotation?, *EPL* **103**, 57008 (2013).
- [17] F. Wilczek, Wilczek reply, *Phys. Rev. Lett.* **110**, 118902 (2013).
- [18] T. Li, Z.-X. Gong, Z.-Q. Yin, H.T. Quan, X. Yin, P. Zhang, L.-M. Duan, and X. Zhang, Reply to Comment on “Space-time crystals of trapped ions,” arXiv:1212.6959v2.
- [19] H. Watanabe and M. Oshikawa, Absence of quantum time crystals, *Phys. Rev. Lett.* **114**, 251603 (2015).
- [20] K. Sacha, Modeling spontaneous breaking of time-translation symmetry, *Phys. Rev. A* **91**, 033617 (2015).
- [21] V. Khemani, A. Lazarides, R. Moessner, and S.L. Sondhi, Phase structure of driven quantum systems, *Phys. Rev. Lett.* **116**, 250401 (2016).

- [22] D.V. Else, B. Bauer, and C. Nayak, Floquet time crystals, *Phys. Rev. Lett.* **117**, 090402 (2016).
- [23] N.Y. Yao, A.C. Potter, I.D. Potirniche, and A. Vishwanath, Discrete time crystals: Rigidity, criticality, and realizations, *Phys. Rev. Lett.* **118**, 030401 (2017).
- [24] A. Russomanno, F. Iemini, M. Dalmonte, and R. Fazio, Floquet time crystal in the Lipkin-Meshkov-Glick model, *Phys. Rev. B* **95**, 214307 (2017).
- [25] E. Gibney, The quest to crystallize time, *Nature* **543**, 164 (2017).
- [26] J. Zhang, P.W. Hess, A. Kyprianidis, P. Becker, A. Lee, J. Smith, G. Pagano, I.-D. Potirniche, A.C. Potter, A. Vishwanath, N.Y. Yao, and C. Monroe, Observation of a discrete time crystal, *Nature* **543**, 217 (2017).
- [27] S. Choi, J. Choi, R. Landig, G. Kucsko, H. Zhou, J. Isoya, F. Jelezko, S. Onoda, H. Sumiya, V. Khemani, C. von Keyserlingk, N.Y. Yao, E. Demler, and M.D. Lukin, Observation of discrete time-crystalline order in a disordered dipolar many-body system, *Nature* **543**, 221 (2017).
- [28] See also the Supplemental Material of Ref. [13].
- [29] C. Yannouleas and U. Landman, Symmetry breaking and quantum correlations in finite systems: Studies of quantum dots and ultracold Bose gases and related nuclear and chemical methods, *Rep. Prog. Phys.* **70**, 2067 (2007).
- [30] J. Sato, R. Kanamoto, E. Kaminishi, and T. Deguchi, Exact relaxation dynamics of a localized many-body state in the 1D Bose gas, *Phys. Rev. Lett.* **108**, 110401 (2012).
- [31] G. Eriksson, J. Bengtsson, E.Ö. Karabulut, G.M. Kavoulakis, and S.M. Reimann, Bose-Einstein condensates in a ring potential: Time-evolution beyond the mean-field approximation, arXiv:1706.00859v1.
- [32] A.I. Streltsov, O.E. Alon, and L.S. Cederbaum, Swift loss of coherence of soliton trains in attractive Bose-Einstein condensates, *Phys. Rev. Lett.* **106**, 240401 (2011).
- [33] Ch. Weiss and L.D. Carr, Higher-order quantum bright solitons in Bose-Einstein condensates show truly quantum emergent behavior, arXiv:1612.05545.
- [34] G.C. Katsimiga, G.M. Koutentakis, S.I. Mistakidis, P.G. Kevrekidis, and P. Schmelcher, Darkbright soliton dynamics beyond the mean-field approximation, *New J. Phys.* **19**, 073004 (2017).
- [35] Wave packet dispersion was also reported in a recent study of inhomogeneous spin configurations on a ring of N bosonic ions, F. Robicheaux and K. Niffenegger, Quantum simulations of a freely rotating ring of ultracold and identical bosonic ions, *Phys. Rev. A* **91**, 063618 (2015).
- [36] C. Yannouleas and U. Landman, Strongly correlated wave functions for artificial atoms and molecules, *J. Phys.: Condens. Matter* **14**, L591 (2002).
- [37] C. Yannouleas and U. Landman, Trial wave functions with long-range Coulomb correlations for two-dimensional N -electron systems in high magnetic fields, *Phys. Rev. B* **66**, 115315 (2002).
- [38] C. Yannouleas and U. Landman, Two-dimensional quantum dots in high magnetic fields: Rotating-electron-molecule versus composite-fermion approach, *Phys. Rev. B* **68**, 035326 (2003).
- [39] C. Yannouleas and U. Landman, Group theoretical analysis of symmetry breaking in two-dimensional quantum dots, *Phys. Rev. B* **68**, 035325 (2003).
- [40] C. Yannouleas and U. Landman, Unified description of floppy and rigid rotating Wigner molecules formed in quantum dots, *Phys. Rev. B* **69**, 113306 (2004).
- [41] I. Romanovsky, C. Yannouleas, and U. Landman, Crystalline boson phases in harmonic traps: Beyond the Gross-Pitaevskii mean field, *Phys. Rev. Lett.* **93**, 230405 (2004).
- [42] Y. Li, C. Yannouleas, and U. Landman, From a few to many electrons in quantum dots under strong magnetic fields: Properties of rotating electron molecules with multiple rings, *Phys. Rev. B* **73**, 075301 (2006).
- [43] I. Romanovsky, C. Yannouleas, and U. Landman, Edge states in graphene quantum dots: Fractional quantum Hall effect analogies and differences at zero magnetic field, *Phys. Rev. B* **79**, 075311 (2009).
- [44] C. Yannouleas and U. Landman, Unified microscopic approach to the interplay of pinned-Wigner-solid and liquid behavior of the lowest Landau-level states in the neighborhood of $\nu = 1/3$, *Phys. Rev. B* **84**, 165327 (2011).
- [45] R.E. Peierls and J. Yoccoz, The collective model of nuclear motion, *Proc. Phys. Soc. (London) A* **70**, 381 (1957).
- [46] P. Ring and P. Schuck, *The Nuclear Many-Body Problem*, (New York, Springer, 1980) ch. 11.
- [47] P.-O. Löwdin, Quantum theory of many-particle systems: III. Extension of the Hartree-Fock scheme to include degenerate systems and correlation effects, *Phys. Rev.* **97**, 1509 (1955).
- [48] R. Rodríguez-Guzmán, J.L. Egido, and L.M. Robledo, Correlations beyond the mean field in Magnesium isotopes: Angular momentum projection and configuration mixing, *Nucl. Phys. A* **709**, 201 (2002).
- [49] M. Bender, P.-H. Heenen, and P.-G. Reinhard, Self-consistent mean-field models for nuclear structure, *Rev. Mod. Phys.* **75**, 121 (2003).
- [50] H. Zduńczuk, W. Satuła, J. Dobaczewski, and M. Kosmowski, Angular momentum projection of cranked Hartree-Fock states: Application to terminating bands in $A \sim 44$ nuclei, *Phys. Rev. C* **76**, 044304 (2007).
- [51] Y. Sun, Projection-technique approach to the nuclear many-body problem, *Phys. Scr.* **91**, 043005 (2016).
- [52] J.A. Sheikh and P. Ring, Symmetry-projected Hartree-Fock-Bogoliubov equations, *Nucl. Phys. A* **665**, 71 (2000).
- [53] W. Satuła, J. Dobaczewski, W. Nazarewicz, and T.R. Werner Isospin-breaking corrections to superallowed Fermi β decay in isospin- and angular-momentum-projected nuclear density functional theory, *Phys. Rev. C* **86**, 054316 (2012).
- [54] G. Giuliani and G. Vignale, *Quantum Theory of the Electron Liquid* (Cambridge University Press, Cambridge, 2008) ch 1.6
- [55] P.C. Lichtner and J.J. Griffin, Evolution of a quantum system: Lifetime of a determinant, *Phys. Rev. Lett.* **37**, 1521 (1976).
- [56] K. Maki and X. Zotos, Static and dynamic properties of a two-dimensional Wigner crystal in a strong magnetic field, *Phys. Rev. B* **28**, 4349 (1983).
- [57] L.D. Landau and E.M. Lifshitz, *Course of Theoretical Physics*, Vol. 9, Statistical Physics, Part 2 (Pergamon Press, Oxford, 1980) p. 248.
- [58] R.E. Peierls, Zur theorie des diamagnetismus von leitungselektronen, *Z. Physik* **80**, 763 (1933).
- [59] A.B. Wolbarst, *Symmetry and Quantum Systems* (Van Nostrand Reinold, New York, 1977).
- [60] F.A. Cotton, *Chemical Applications of Group Theory*, (Wiley, New York, 1990).

- [61] M. Hamermesh, *Group Theory and its Application to Physical Problems* (Addison-Wesley, Reading, MA, 1962).
- [62] A.C. Hurley, *Introduction to the Electron Theory of Small Molecules* (Academic Press, London, 1976) ch. 6.
- [63] K. Ishida, Molecular integrals over the gauge-including atomic orbitals, *J. Chem. Phys.* **118**, 4819 (2003).
- [64] S.F. Boys, Electronic wave functions. I. A general method of calculation for the stationary states of any molecular system, *Proc. R. Soc. (London) Ser. A* **200**, 542 (1950).
- [65] C. Yannouleas and U. Landman, to be published.
- [66] C. Yannouleas and U. Landman, Collective and independent-particle motion in two-electron artificial atoms, *Phys. Rev. Lett.* **85**, 1726 (2000).
- [67] R. Kanamoto, L.D. Carr, and M. Ueda, Topological winding and unwinding in metastable Bose-Einstein condensates, *Phys. Rev. Lett.* **100**, 060401 (2008).
- [68] R. Kanamoto, L.D. Carr, and M. Ueda, Metastable quantum phase transitions in a periodic one-dimensional Bose gas: Mean-field and Bogoliubov analyses, *Phys. Rev. A* **79**, 063616 (2009).
- [69] R. Kanamoto, L.D. Carr, and M. Ueda, Metastable quantum phase transitions in a periodic one-dimensional Bose gas. II. Many-body theory, *Phys. Rev. A* **81**, 023625 (2010).
- [70] Å. Bohr & B.R. Mottelson, *Nuclear Structure*, (World Scientific, Singapore, 1998) Vol. II.
- [71] W.Y. Ruan, Y.Y. Liu, C.G. Bao, and Z.Q. Zhang, Origin of magic angular momenta in few-electron quantum dots, *Phys. Rev. B* **51**, 7942 (1995).
- [72] P.A. Maksym, Eckardt frame theory of interacting electrons in quantum dots, *Phys. Rev. B* **53**, 10871 (1996).
- [73] T. Seki, Y. Kuramoto, and T. Nishino, Origin of magic angular momentum in a quantum dot under strong magnetic field, *J. Phys. Soc. Japan.* **65**, 3945 (1996).
- [74] P.A. Maksym, H. Imamura, G.P. Mallon, and H. Aoki, Molecular aspects of electron correlation in quantum dots, *J. Phys.: Condens. Matter* **12**, R299 (2000).
- [75] P. Bocchieri and A. Loinger, Quantum recurrence theorem, *Phys. Rev.* **107**, 337 (1957).
- [76] L. S. Schulman, Note on the quantum recurrence theorem, *Phys. Rev. A* **18** 2379 (1978).
- [77] H. Che, K. Deng, Z.T. Xu, W.H. Yuan, J. Zhang, and Z.H. Lu, Efficient Raman sideband cooling of trapped ions to their motional ground state, *Phys. Rev. A* **96**, 013417 (2017).